A Hybrid Analytical-Numerical Model of Heat Generation and Distribution in Friction Stir Welded AA2024 Butt Joints

Mohamed M. El-Sayed Seleman[1], Ahmed M. Elnaml[1]*, Sabbah Ataya[1,2], Mohamed M. Z. Ahmed[3], Sarah A. Elnekhaily[1], Khalid M. Hafez[4]

[1] Department of Metallurgical and Materials Engineering, Faculty of Petroleum and Mining Engineering,
    Suez University, 43512 Suez, EGYPT

[2] Department of Mechanical Engineering, College of Engineering,
    Imam Mohammad Ibn Saud Islamic University, Riyadh 11432, SAUDI ARABIA

[3] Mechanical Engineering Department, College of Engineering at Al Kharj,
    Prince Sattam Bin Abdulaziz University, Al Kharj 16273, SAUDI ARABIA

[4] Central Metallurgical Research and Development Institute (CMRDI),
    P.O. Box 87, Helwan 11421, EGYPT

*Corresponding Author: ahmedelnaml94@gmail.com
DOI: https://doi.org/10.30880/ijie.2024.16.05.0012

Abstract

Being a solid-state process, friction stir welding (FSW) is considered a candidate technique for welding critically-microstructure-sensitive materials such as heat-treatable aluminum alloys. A hybrid computational model that employs both analytical and numerical approaches was used to estimate the amount of heat generated in the FSW of AA2024-T4 butt-welded sheets and how it is distributed as a function of time using a 3D transient heat transfer finite element analysis (FEA). Experimental procedures were used to validate the heat distribution in the welded butt joints using candidate rotational and travel speeds from the numerical model. The model outcomes show that rotational speed less than 600 rpm gives insufficient heat input when the optimum travel speed is 25 mm/min while higher rpm would cause overheating and flash formation. Structural and mechanical joint characterizations were performed to ensure the validity of the optimized process parameters. The model recommended parameters give the defect-free butt joints with the best efficiency in terms of ultimate strength. The Vickers hardness profile (W-shaped) for the welds' cross-sections shows that 600 rpm gives the highest values in all different weld zones compared to that welded at 400 and 800 rpm.

1. Introduction

Friction stir welding (FSW) is considered a thermomechanical solid-state welding process in which joining occurs in the solid state [1, 2]. There is an ongoing worldwide demand for solid-state welding procedures, in general, to overcome some problems encountered with traditional fusion techniques such as micro and macro segregation, large heat inputs, shrinkage porosities, welding cracking, and so on. Moreover, minor microstructural changes may occur in comparison with fusion welding, in which complete melting and solidification take place [2].

Nomenclature

FSW	Friction Stir Welding
SZ	Stir Zone
HAZ	Heat Affected Zone
TMAZ	Thermo-Mechanically Affected Zone
T4	Naturally aged after a solution heat treatment.
AS	Advancing Side
RS	Retreating Side
δ	Contact state variable
ω	Angular velocity of the tool (rad/s)
$\tau_{contact}$	Contact shear stress (MPa)
M	Rotational Torque (N.m)
T_{yield}	Yield shear stress (MPa)
α	Conical angle in radians
μ	Friction coefficient
Q	Amount of heat generated (J)
R_{probe}	The radius of the probe
$R_{shoulder}$	The radius of the shoulder
h	Convection heat transfer coefficient
rpm	Revolution Per Minutes
FEM	Finite Element Method
NMSE	The normalized mean square error
T_{mi}	The measured temperature
T_{ni}	The temperature numerically calculated
%EL	Percent of Elongation
VHN	Vickers Hardness Number

During the FSW, the temperature is expected to be asymmetric around the weld centerline, so the weld's two sides are distinguished [3, 4]. The side where the tangential velocity is in a direction with the travel velocity is called the advancing side (AS), while the other is called the retreating side (RS) [4, 5], as illustrated in **Fig. 1**. Aval et al. showed that, the material behavior within each side is expected to be different as a result of the created temperature asymmetry [5]. In addition, different welding regions undergo unsimilar heating and cooling rates that eventually affect their mechanical properties [6–8].
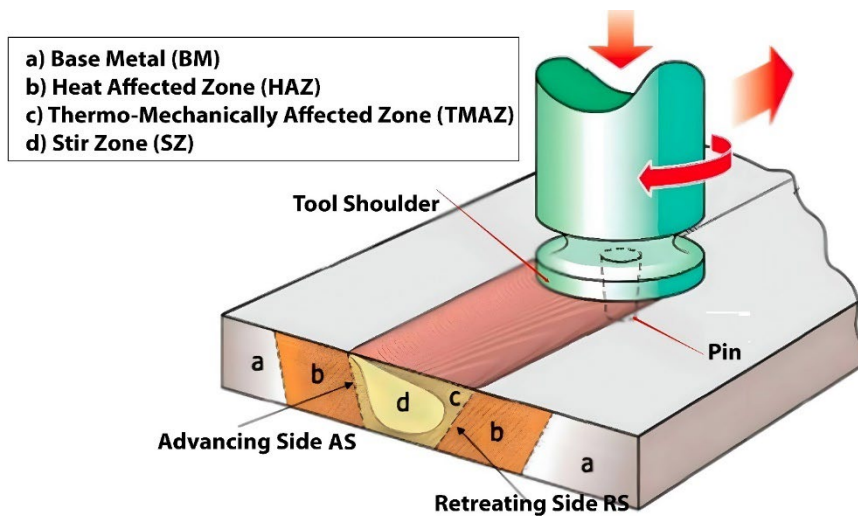

Fig. 1 *FSW process with different weld regions [9]*

The unsymmetrical temperature distribution between the two sides affects the flow of the material around the tool; besides, different welding regions are exposed to different heating and cooling rates, and thus different mechanical properties are expected [7, 8]. Friction heats the material to sufficiently high temperatures; thus, the metal below and around the tool softens [10, 11]. With an adequate amount of plastic deformation, dynamic recrystallization could take place from which some microstructural features, especially the grain size, could be altered [12-14]. Babu & Karunakaran et al. reported that different regions of the workpiece are exposed to

different temperatures. So, as a result of this uneven heat distribution, different welding regions are exposed to different heating and cooling rates [14].

The tool design and geometry play a critical role in the welding process. They have a direct effect on metal flow in both the weld zone and the thermo-mechanically affected zone (TMAZ) [15, 16]. They, thus, have a noticeable influence on the quality of the weld and the established microstructure [10,15,18]. For example, several researchers reported that the tool should not be at an exact right angle to the workpiece but tilted at an angle of 2-4° to help in the metal forging action [17–19].

During FSW, heat distribution is affected not only by conductive heat transfer but also by mass transfer and by the metal flow that occurs in both the weld zone and the TMAZ [15, 16]. Different parameters should be considered and optimized for a highly efficient welding process, such as travel speed, rotational speed, tool plunge depth , tilt angle, the tool design/features, and the weld material [20]. The tool design and its geometry have a significantly critical role in the welding process and have a very noticeable influence on the quality of the weld [10, 14]. So, the design of the tool has a critical role in the optimization of the welding parameters [14]. The microstructural features evolved after welding, the material flow around the tool, and the interfacial heat generation, are affected by the design of the tool [14]. In addition, the plunge depth should be considered an important welding parameter. Insufficient plunge depth can result in lower pressure at the contact interface of the workpiece and tool shoulder, which reduces the heat generated at the welding interface and lowers both the efficiency and quality of the weld [21, 22]. On the contrary, higher plunge depths may reduce weld thickness.

Muhsin et al. reported that higher tool rotational speeds and lower travel speeds result in higher heat generation [23]. Higher rotational speed and lower welding speeds can result in a wider heat affected zone (HAZ) and coarser grains [24].Therefore, care should be taken to avoid extensive and unfavorable microstructural features. On the other extreme, if the heat generated is quite insufficient, complete joining would not be ensured [25, 26].

Yang et al. showed that the physical interactions occurring during the FSW process are highly complex due to their dependency on the applied thermo-mechanical treatment, material flow, and heat transfer [27]. All these interactions affect each other and, subsequently, affect the microstructural features evolved in both HAZ and weld zones [13, 28], which govern the mechanical properties of the joint and its efficiency [29].

The amount of heat generated and transferred to the HAZ determines the maximum rise in temperature, the duration of the temperature rise, and the rate of its cooling [30, 31]. There has been significant interest to reveal the numerous aspects of the FSW process and understanding the underlying mutual relationships between the welding parameters and their impact on the mechanical properties of the welded joint [32, 33]. Unfortunately, there are experimental restrictions to uncover all the changes that take place in the material in real-time and the evolved microstructural changes or even just heat distribution at specific points [25]. Therefore, developing computational models is still a challenge and a hot topic to help predict the material behaviors during the FSW process and hence optimize the welding parameters towards better joint quality and performance. And also, to better understand and reveal the physical and mechanical changes occurring in real-time [27, 34, 35]. Even though several friction stir-welded aluminum alloys have been successfully studied, the FSW of the 2xxx aluminum alloy series is still an area of interest for more research as their applications are widely spread in the aviation industry and advanced means of transportation, especially AA2024 aluminum [25].

Thus, the aim of this research is to develop and implement a comprehensive numerical-analytical hybrid computational model to predict heat transfer in different welding zones and how it is affected by key welding process parameters like rotational and travel speeds during the FSW process of AA 2024 alloy. The heat generation and distribution, as well as their influence on microstructural changes and the mechanical properties of the AA2024-T4 similar butt joints in light of the proposed model were investigated and discussed.

2. Materials and Methods

2.1 Workpiece Material

The material used in our study was AA 2024-T4 alloy as a typical representative of 2xxx aluminum alloys. For the plastic deformation behavior, we use the Johnson-Cook model [36–38], where the flow stress (σ_y) is a function of strain rate ($\dot{\varepsilon}_p$) , equivalent amount of strain (ε_p), and the working temperature (T).

$$\sigma_y = \left[A + B\left(\varepsilon_p\right)^n\right]\left[1 + C\ ln\left(\frac{\dot{\varepsilon}_p}{\dot{\varepsilon}_o}\right)\right]\left[1 - \left(\frac{T - T_o}{T_{melt} - T_o}\right)^m\right] \tag{1}$$

With Johnson-Cook material constants for AA 2024-T4, A= 369 MPa , B= 684 MPa , n= 0.73 , C= 0.0083 , m= 1.7 , Tmelt = 502°C and reference temperature To = 25°C [39] where $\dot{\varepsilon}_o$ is a reference strain rate. Heat dissipation during the FSW welding is expected to be very complex as it depends not only on the thermal conductivity of the weld material, but also on its specific heat and density, considering the fact that it is a transient heat transfer

problem [27, 40]. The thermal properties of AA2024-T4 (the specific heat and thermal conductivity) as determined by Sarmast et al. [39–41] are chosen, analyzed and plotted as a function of temperature, see Fig. *2*. The chemical composition of the AA 2024 alloy is shown in Table 1 as taken from the material supplier (The aluminum Company of Egypt, Egyptalum) datasheet:

Table 1 *Chemical composition of the AA 2024-T4 alloy*

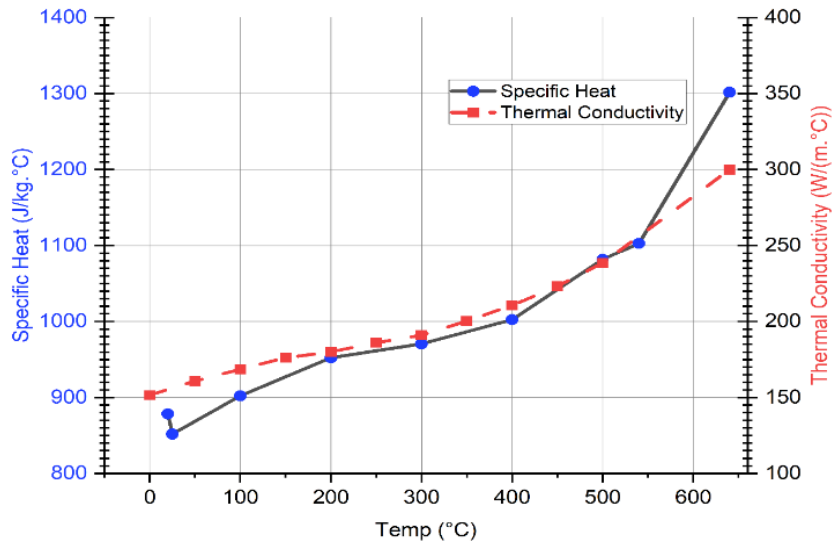| Si	Fe	Cu	Mn	Mg	Cr	Zn	Ti	Al
0.5%	0.5%	3.8-4.9%	0.30-0.9%	1.2-1.8%	0.1%	0.25%	0.15%	Bal.

Fig. 2 *Specific heat and thermal conductivity temperature-dependency of AA2024-T4 aluminium alloy*

2.2 Tool Geometry

The geometrical characteristics of the tool are very critical since they affect the amount of generated heat and its distribution [30, 33, 42]. It should be effectively designed so that the weld is complete and defect-free as much as possible. The design typically affects the amount of stirring and mixing beneath the tool [33, 40]. **Fig. 3** shows the dimensions of the tool used in the present model.
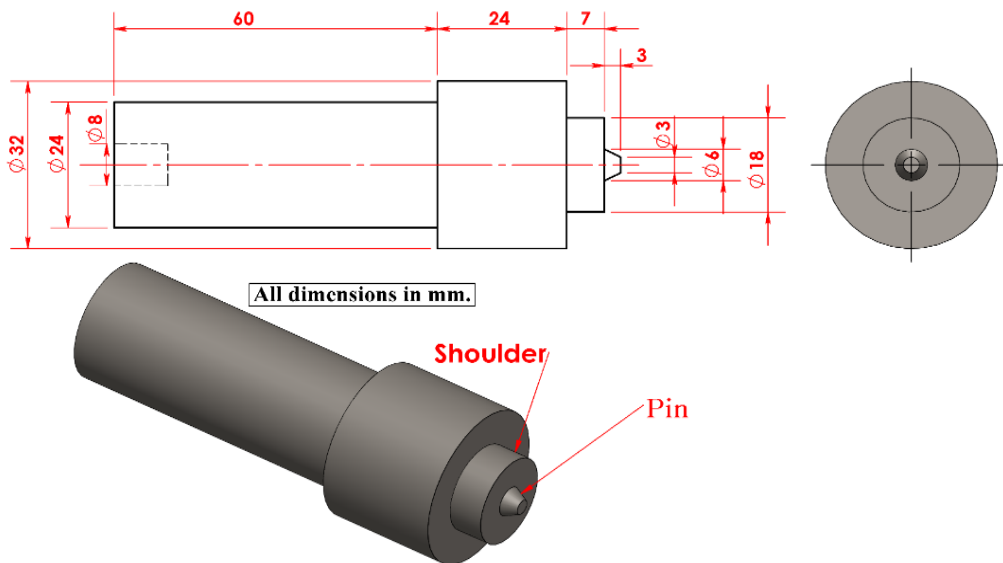

Fig. 3 *FSW tool dimensions*

2.3 Tool Materials

Due to the severe friction evolved in the process, the tool material should have high mechanical properties such as wear resistance and impact resistance to withstand the high rotational speed, as well as high strength and

toughness at all expected elevated temperatures in the weld zone [29, 43]. These high mechanical properties should assure a negligible amount of plastic deformation compared to that of the workpiece [22, 44]. High-speed steels are found to be suitable candidates, especially for welding aluminum alloys [45, 46]. In addition, the thermal behavior of the tool material affects the heat partitioning between the tool and the workpiece, as Equation (2) estimates the fraction of heat partitioned to the workpiece[45, 47].The tool was made of H13 chromium hot-work tool steel.

$$f_w = \frac{\sqrt{(k\rho C_p)_w}}{\sqrt{(k\rho C_p)_w} + \sqrt{(k\rho C_p)_t}}$$
(2)

Where:

f : is the heat partitioned fraction to the workpiece.
k : is the thermal conductivity
C_p: is the specific heat.
ρ: is the material density

and the subscripts w and t refer to the workpiece and tool, respectively.

2.4 Welding Conditions

The welding is performed on a full-automatic FSW machine (Model: EG-1 FSW/FSP, SSMMR-CSE, Suez, Egypt). The 4 mm sheet material of AA 2024-T4 aluminum alloy was cut into plates with 100 mm length and 100 mm width. The plates were clamped on the worktable of the FSW machine. Rotational speeds of 400, 600 and 800 rpm, with a travel speed of 25 mm/min, were used as the main welding parameters to produce the similar AA2024-T4 butt joints. A higher rotation speed of 1000 rpm was excluded from experimental verification since the numerical simulation results showed excessive heat generation. The generated heat during welding is qualitatively monitored at the surface just behind the tool using a dual laser infrared Thermometer (Model: Extech 42570). Also, 4 K-type thermocouples were used to measure the temperature every 500 ms at hole locations, as shown in Fig. 4.

2.5 Joint Characterization

Metallographic analyses of the joints' cross-sections were carried out through optical microscopic images that are generated using the OLYMPUS upright metallurgical microscope BX53M (Tokyo, Japan) after grinding, polishing, and etching with Keller's reagent. On the other hand, mechanical characterization was performed by tensile and hardness tests. The tensile test was conducted using a universal tensile testing machine (Model WDW-300D, Guangdong, China) with a 0.05 mm/sec crosshead speed. The tested specimens were cut from the welded sheets as per ASTM E8 for metallic sheets, as shown in Fig. 5. The Vickers hardness test was conducted using a load of 0.5 Kg at a constant holding time of 15 s for the weld cross-sections using the QNESS hardness tester (Q10 M, Mammelzen, Germany). The locations of the samples used for joint characterization are displayed in Fig. 4.
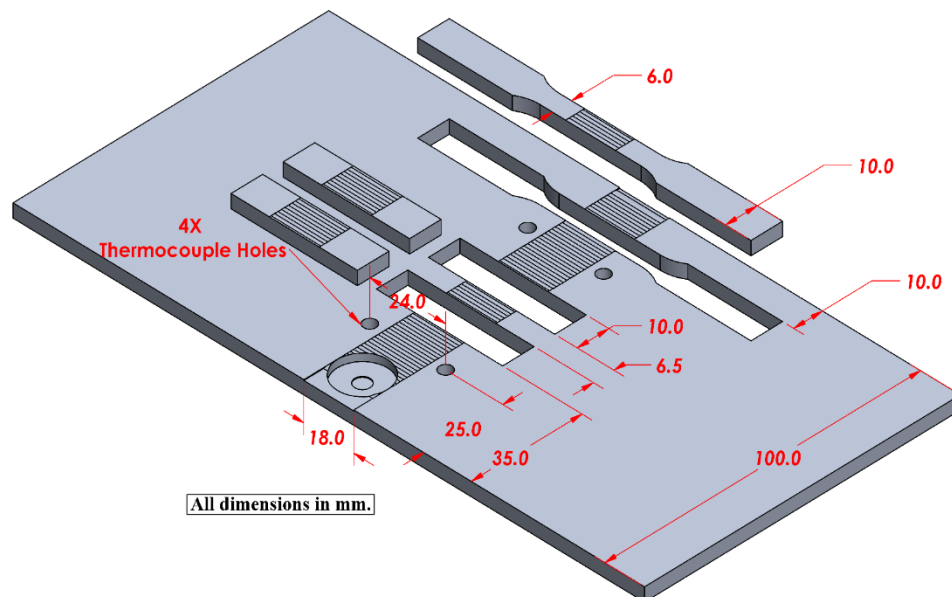

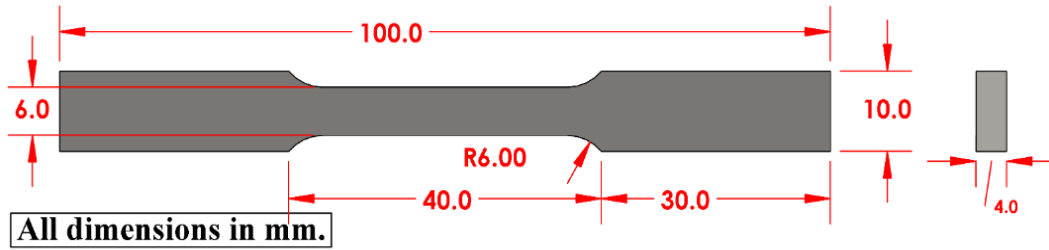**Fig. 4** *Tensile, hardness, and microscopy specimens' locations*

Fig. 5 *A standard tensile test specimen according to ASTM E8*

3. Modeling Approach

3.1 Mathematical Modeling of Heat Generation

The amount of heat generated is estimated mathematically using a torque-based method, assuming that friction is the main source of heat generation [17, 48, 49]. For the contact between the tool and the workpiece, the Coulomb friction law is used to estimate the shearing interface stress [17, 50]. Two friction conditions are expected (sliding and sticking), if the friction shear stress exceeds the yield shear stress of the workpiece, the sticking condition will prevail [51, 52], otherwise, sliding would occur. But if the contact shear is in the range of the yield stress, then the friction condition can be partial sliding/sticking. A Contact state variable δ is used to define the extent of the sticking friction as a fraction (ranging from 0 for sliding to 1 for complete sticking) [51–53]. During the FSW welding phase, heat is generated at the contact surface (Fig. 6 shows the volume element for the vertical surface), depending on the geometry of the tool (simplified as a conical or horizontal shoulder) [37, 48, 54]. So, It is assumed that the generated heat is divided into three components, Q_1, Q_2 and Q_3 [55, 56]:

Where:

- Q_1: is the heat generated under the tool shoulder.
- Q_2: is the heat generated at the tool probe side.
- Q_3: is the heat generated at the tool probe tip.

Then, the total heat generated $Q_{\text{total}} = Q_1 + Q_2 + Q_3$.

The notation for directions used is:

- $—$: Horizontal (perpendicular to the rotation axis, circular surface).
- $|$: Vertical (parallel to the rotation axis, cylindrical surface).
- $\backslash$: Conical (tilted with respect to the rotation axis, conical surface).
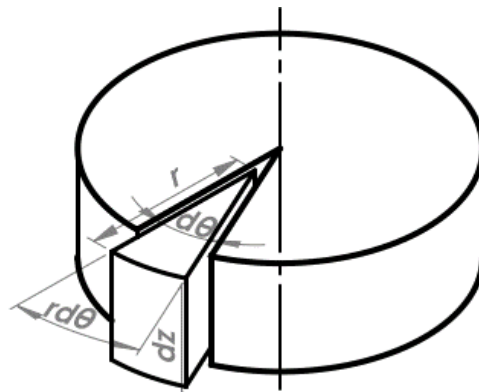

Fig. 6 *Volume element of the vertical surface*

To estimate the amount of heat generated, uniform contact stress is assumed:

$$dQ = \omega\, dM = \omega r dF = \omega r \tau_{\text{contact}}\, dA \tag{3}$$

Where the contact stress cannot be greater than the flow stress of the workpiece material as determined from Johnson-Cook model Equation (1)[57].

For the horizontal surface:

$$dA_- = r\, d\theta dr \tag{4}$$

$$dQ_- = \omega r dF_- = \omega r^2 \tau_{\text{contact}}\, d\theta dr \tag{5}$$

For the vertical surface:

$$A_| = r\, d\theta\, dz = r\, d\theta\, \tan\alpha\, dz \tag{6}$$

$$dQ_| = \omega r dF_| = \omega \tau_{\text{contact}} r^2 d\theta dz \tag{7}$$

Force on conical faces can be considered as the summation of two components:

$$F_\backslash = dF_- + dF_| \tag{8}$$

$$dz = \tan\alpha\, dr \tag{9}$$

where α is the cone angle for the pin. and the force on the conical surface ($F_\backslash$) is a summation of its two components (vertical and horizontal).

$$dA_| = rd\theta dz = rd\theta \tan\alpha\, dr \tag{10}$$

$$\begin{aligned} dF_\backslash &= \tau_{\text{contact}}\, dA_- + \tau_{\text{contact}}\, dA_| \\ &= \tau_{\text{contact}}\, rd\theta\, dr(1 + \tan\alpha) \end{aligned} \tag{11}$$

$$dQ_\backslash = \omega r dF_\backslash = \omega r^2 \tau_{\text{contact}}\, d\theta dr(1 + \tan\alpha) \tag{12}$$

For the shoulder area, we integrate Equation (*12*) from R_{probe} to $R_{shoulder}$:

$$\begin{aligned} Q_1 &= \int_0^{2\pi} \int_{R_{\text{probe}}}^{R_{\text{shoulder}}} \omega\, \tau_{\text{contact}}\, r^2(1 + tan\alpha)dr\, d\theta \\ &= \frac{2}{3}\pi\tau_{\text{contact}}\, \omega\big(R_{\text{shoulder}}^3 - R_{\text{probe}}^3\big)(1 + tan\alpha) \end{aligned} \tag{13}$$

For the probe (vertical) area, we integrate Equation (*7*) from 0 to H_{probe}:

$$\begin{aligned} Q_2 &= \int_0^{2\pi} \int_0^{H_{\text{probe}}} \omega\, \tau_{\text{contact}}\, R_{\text{probe}}^2\, dz\, d\theta \\ &= 2\pi\tau_{\text{contact}}\, \omega R_{\text{probe}}^2 H_{\text{probe}} \end{aligned} \tag{14}$$

For the probe area, we integrate Equation (*12*) from 0 to R_{probe}:

$$\begin{aligned} Q_3 &= \int_0^{2\pi} \int_0^{R_{\text{probe}}} \omega\, \tau_{\text{contact}}\, r^2(1 + tan\alpha)\, dr\, d\theta \\ &= \frac{2}{3}\pi_{\text{contact}}\, \omega R_{\text{probe}}^3 (1 + tan\alpha) \end{aligned} \tag{15}$$

$$\begin{aligned} Q_{total} &= Q_1 + Q_2 + Q_3 \\ &= \frac{2}{3}\pi\omega\tau_{\text{contact}} \left(\big(R_{\text{shoulder}}^3 - R_{\text{probe}}^3\big)(1 + \tan\alpha) + R_{\text{probe}}^3 + 3R_{\text{probe}}^2 H_{\text{probe}}\right) \end{aligned} \tag{16}$$

In the case of the cylindrical (non-conical) tool: $tan\alpha = 0$, hence:

$$Q_{\text{total}} = \frac{2}{3}\pi\omega\tau_{\text{contact}} \left(R_{\text{shoulder}}^3 + 3R_{\text{probe}}^2 H_{\text{probe}}\right) \tag{17}$$

For the sticking condition:

$$\tau_{\text{contact}} = \tau_{\text{yield}} = \frac{\sigma_{\text{yield}}}{\sqrt{3}} \tag{18}$$

$$Q_{\text{total, sticking}} = \frac{2}{3}\pi\omega \frac{\sigma_{\text{yield}}}{\sqrt{3}} \left(\big(R_{\text{shoulder}}^3 - R_{\text{probe}}^3\big)(1 + \tan\alpha) + R_{\text{probe}}^3 + 3R_{\text{probe}}^2 H_{\text{probe}}\right) \tag{19}$$

But for the sliding condition:

$$Q_{\text{total, sliding}} = \frac{2}{3}\pi\omega\mu p\left(\left(R_{\text{shoulder}}^3 - R_{\text{probe}}^3\right)(1 + \tan\alpha) + R_{\text{probe}}^3 + 3R_{\text{probe}}^2 H_{\text{probe}}\right) \tag{20}$$

The total power is transformed almost completely into thermal energy [58]. Finally, for the general case where both types of friction are accounted for:

$$
\begin{aligned}
Q_{\text{total}} &= \delta Q_{\text{total, sticking}} + (1-\delta)Q_{\text{total, sliding}} \\
&= \frac{2}{3}\pi\omega\left(\delta\tau_{\text{yield}} + (1-\delta)\mu p\right)\left(\left(R_{\text{shoulder}}^3 - R_{\text{probe}}^3\right)(1 + \tan\alpha) + R_{\text{probe}}^3 + 3R_{\text{probe}}^2 H_{\text{probe}}\right)
\end{aligned} \tag{21}
$$

3.2 Numerical Model

A 3D finite element model using ABAQUS software was employed to estimate the heat distribution during the dwelling and welding stages. Material properties were defined in the model with the specific heat and thermal conductivity of AA 2024 as a function of temperature, as illustrated in Fig. 2. The total heat input generated during the dwelling and welding is calculated based on Equation (21). It is shown that using a moving heat source is so reliable for model FSW [57]. The heat partitioning between the tool and the workpiece is also considered and calculated using Equation (2). The calculated heat input is fed into the 3D Heat transfer Model using the DFLUX subroutine. Heat transfer hexahedral elements with total number of 74675 are generated with localized seeding along the welding line. Their average aspect ratio equals 1.45.

3.2.1 Boundary Conditions

Both free convection and radiation from the top face of the workpiece are put into account. Considering free convection, the dimensionless Rayleigh number Ra_L is calculated using Equation (22) [59].

$$Ra_L = \frac{g\beta(T_s - T_\infty)L_c^3}{\nu\,\alpha_{th}} \tag{22}$$

$$L_c = \frac{\text{Area}}{\text{perimeter}} = \frac{l * w}{2(l + w)} \tag{23}$$

where:
- α_{th} = thermal diffusivity, m2/s.
- g = gravitational acceleration, m/s^2.
- β = coefficient of volume expansion, 1/K ($\beta = 1/T$: *for ideal gases*).
- T_s = temperature of the surface, ℃.
- T_∞ = temperature of the fluid sufficiently far from the surface, ℃.
- L_c = characteristic length of the geometry, m.
- ν = kinematic viscosity of the fluid, m^2/s.

For laminar flow which is the dominant flow regime in this case, Rayleigh number is used to calculate another dimensionless number (Nusselt) from the empirical relation [60, 61].

$$Nu = 0.59Ra_L^{1/4} \tag{24}$$

The convective heat coefficient (h) is calculated using Equation (25). Table 2 shows a summary of the used values for estimating the (h) coefficient. Air is assumed to be adequately far from the weld surface with a temperature equal to the room temperature (300 K).

$$h = \frac{Nu.k}{L_c} \tag{25}$$

Table 2 *Values used in estimating convective heat transfer coefficient [62]*

Variable	Width	L_c	g	β	T_s	T_∞	k	ν	α_{th}	Ra	Nu	h
Unit	m	m	m/s^2	k^{-1}	k	k	W/ (m.k)	m^2.s^{-1}	m^2.s^{-1}	-----	-----	W/ (m^2.k)
Value	0.1	0.033	9.81	0.0033	400	300	0.025	2.30E-05	5.00E-05	1.05E+05	1.06E+01	7.97

The thermal boundary condition for the specimen surface considers both convective and radiative heat transfer to the surrounding environment using the following Equation (26):

$$k\frac{\partial T}{\partial z}\bigg|_{top} = \sigma\varepsilon(T^4 - T_a^4) + h(T - T_a) \tag{26}$$

where:
- k: the thermal conductivity of the air
- v: the kinematic viscosity of the air
- σ: the Stefan-Boltzmann constant
- ε: the emissivity
- T_a: the ambient temperature in Kelvin.

3.3 Numerical Model Results

Fig. 7 represents the peak temperatures obtained from the solution of the implemented model at selected rotational and travel speeds. These peaks represent the maximum recorded temperatures during the simulation of the welding-path during the welding stage. So, these results serve as a quick FEM-obtained guide that narrows down the search area for the best candidate welding parameters to minimize the experimental required work. **Fig. 7** have showed that higher rotational speeds gives peak temperature close to the melting temperature of the Al2024 (502°C [39]) - at 25 mm/min Travel speed - so that high rpm (1000) are excluded from the experimental verification to avoid excessive heating or localized melting which is not accepted in solid state welding process (FSW) as it would cause defects such as flash formation or improper mixing.
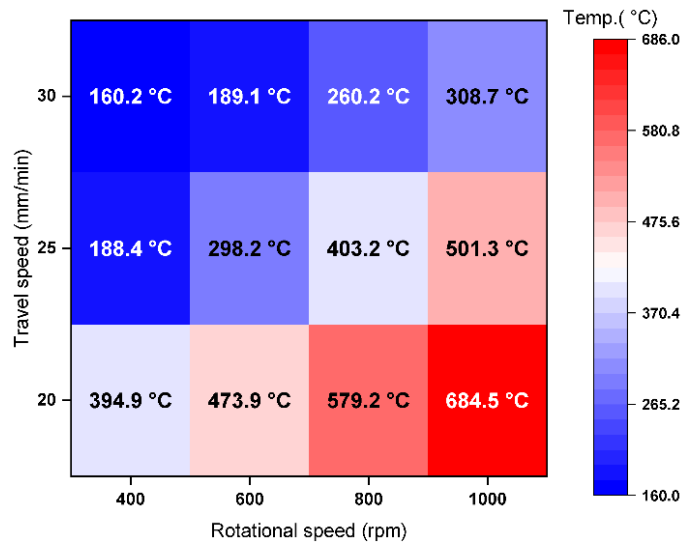

Fig. 7 *Heat map for FEM-determined peak temperatures*

The heat distribution at weld at a certain weld cross-section (75 mm away from the tool entrance face along the welding direction) is shown in Fig. 8 for different rotational speeds (400, 600, 800, and 1000 rpm) and at a travel speed of 25 mm/min. It shows that a higher rotation speed value may cause melting and overheating, and a low rotation speed value is insufficient to cause complete welding. It is also significant to represent the heat distribution profile along a line 1-mm below the top face in the same cross-sections of Fig. 8 of the weld, as shown in Fig. 9.
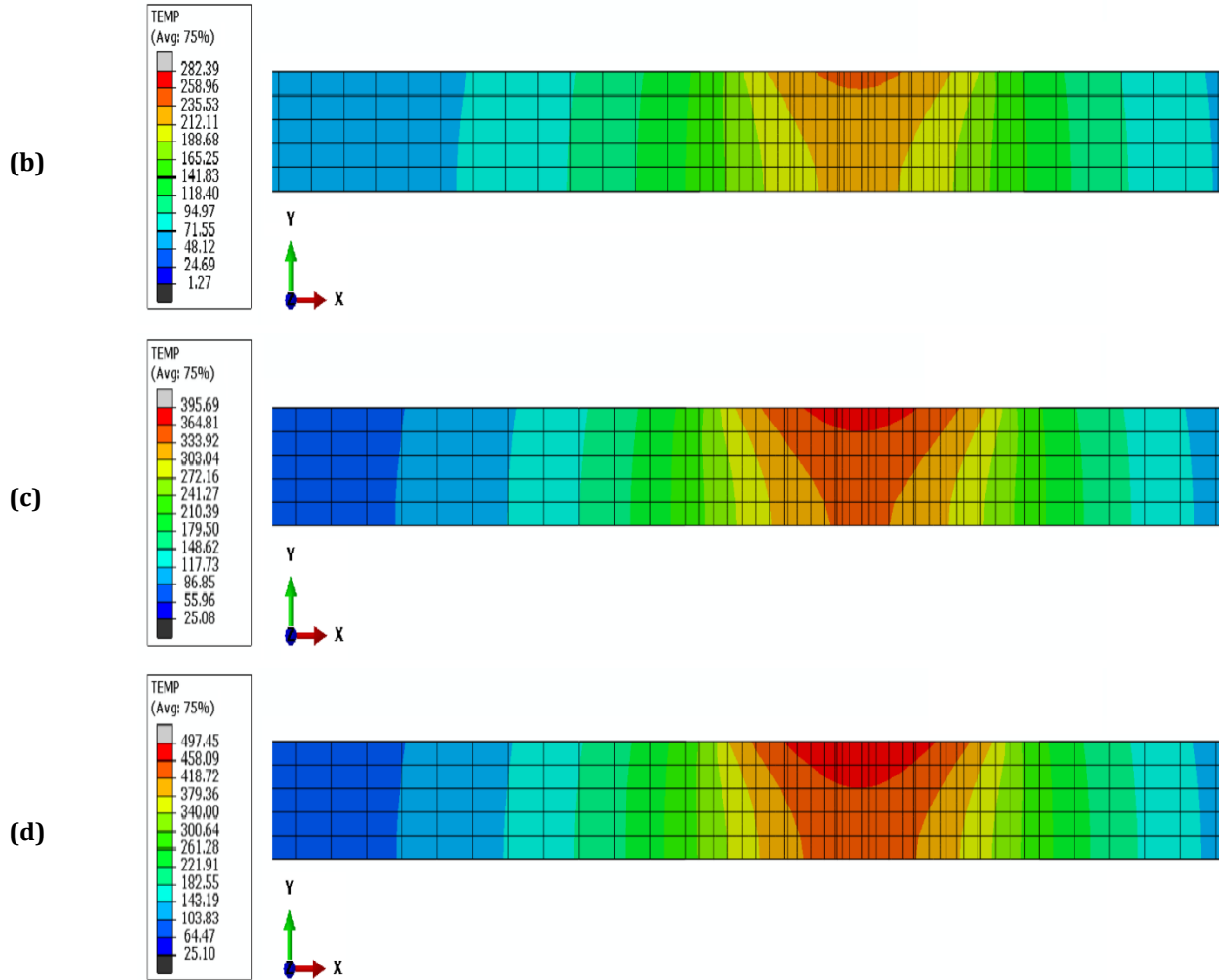
(a)
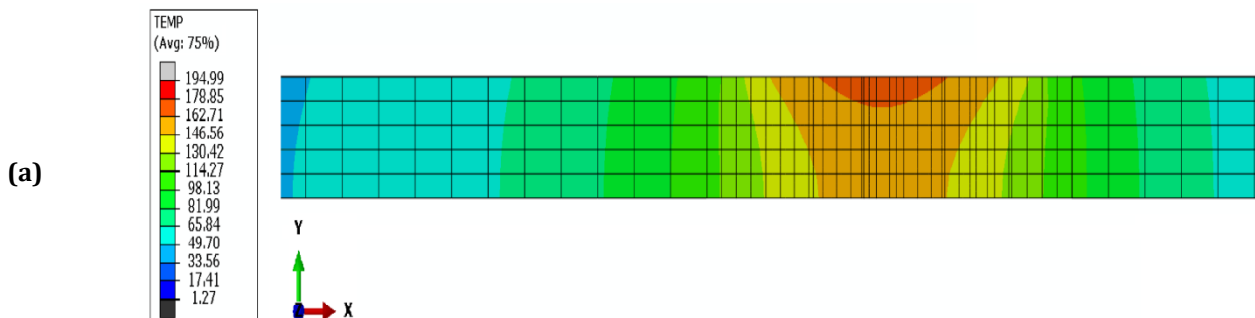
Fig. 8 *Temperature distribution at weld cross-section at a 25 mm/min travel speed and various rotating speeds of (a) 400; (b) 600; (c) 800; (d) 1000 rpm*
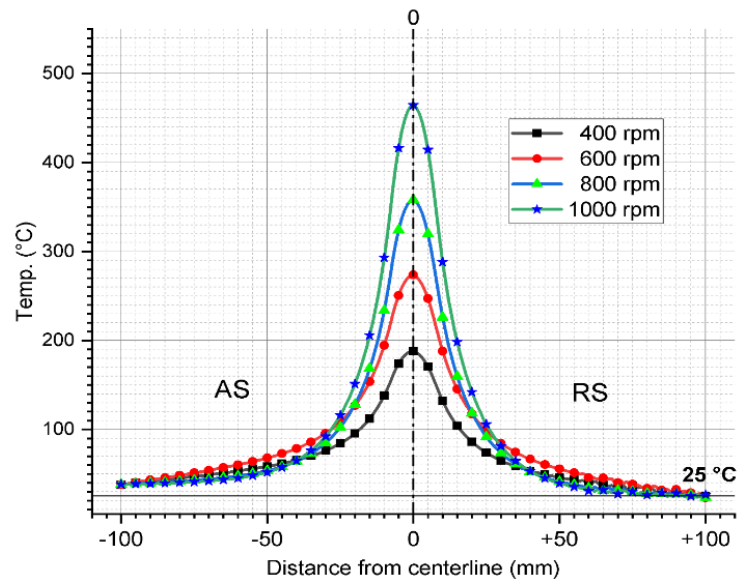

Fig. 9 *Temperature distributions around the weld centerline at various rotation speed values and a 25 mm/min travel speed*

3.3.1 Residual Stress Distribution

It is critical to employ the heat distributions obtained from the heat transfer model to estimate the resultant residual stresses. Modelling residual stress in FSW requires a thermal model followed by an elasto-plastic mechanical one, considering the dependency of the flow stress on temperature , strain amount and strain rate [63]. Fig. 10a shows that a higher rotation speed (1000 rpm) yields higher transverse residual stress in the weld cross-section because of the steepest temperature gradient. Fig. 10b,c shows similar patterns for von Mises and longitudinal stress distributions, respectively.
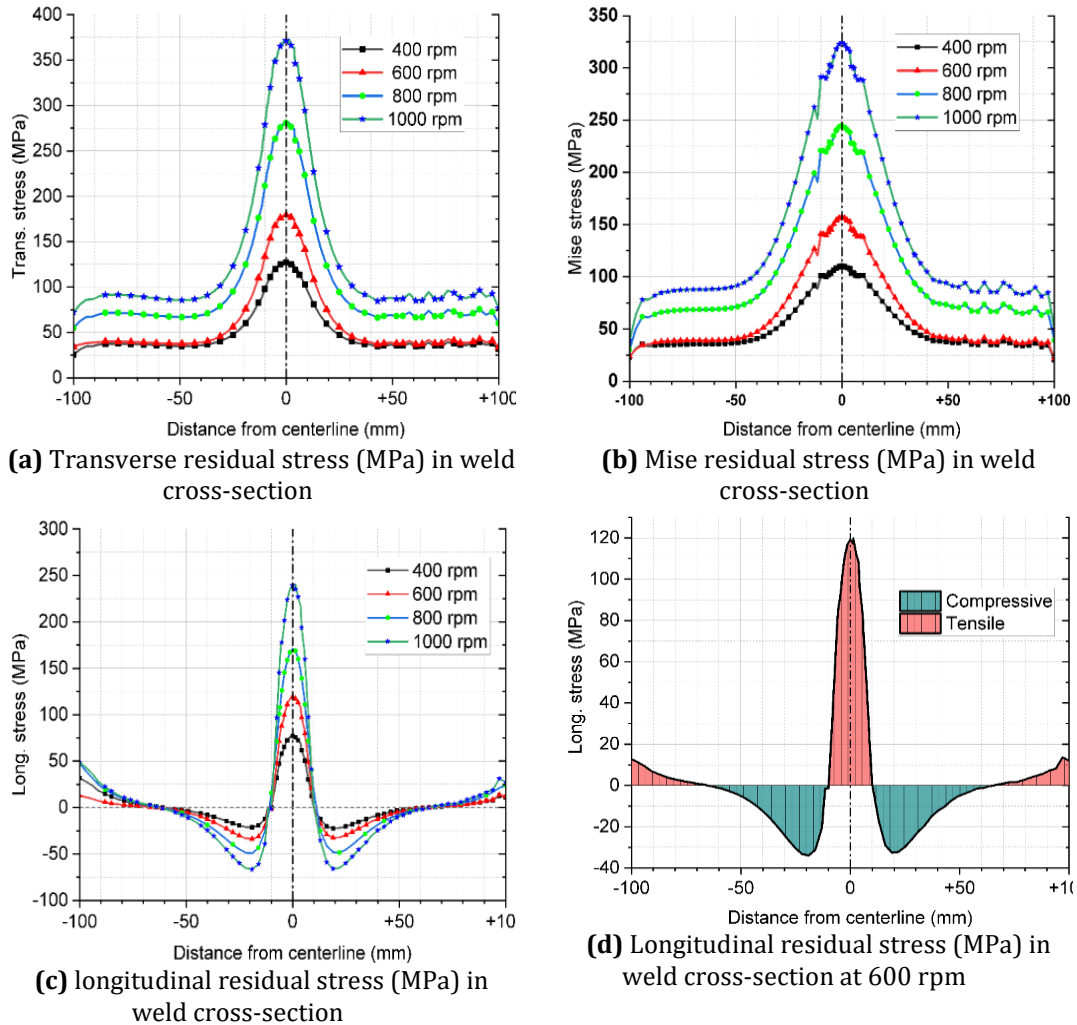
(a) Transverse residual stress (MPa) in weld cross-section

(b) Mise residual stress (MPa) in weld cross-section

(c) longitudinal residual stress (MPa) in weld cross-section

(d) Longitudinal residual stress (MPa) in weld cross-section at 600 rpm

Fig. 10 *Residual stress distribution at welds' cross-sections*

4. Results and Discussion

4.1 Model Validation

The temperatures obtained experimentally and numerically are plotted against time for each welding condition in Fig. 11. It shows a comparison between the temperature obtained experimentally and that obtained from the implemented model as a function of time in seconds. The experimental data is acquired from the k-type thermocouples every 500 milliseconds. Qualitatively, the matching is optimistic. The deviation between the numerically calculated temperature and the measured one is estimated using the normalized mean square error (NMSE) as a model validation metric, as shown in Equation (*27*) [64, 65].

$$MSE = \frac{\sum_i \left(T_{m_i} - T_{n_i}\right)^2}{\sum_i T_{m_i}^2} \tag{27}$$

where: T_{m_i} is measured temperature and T_{n_i} is the numerically calculated temperature.
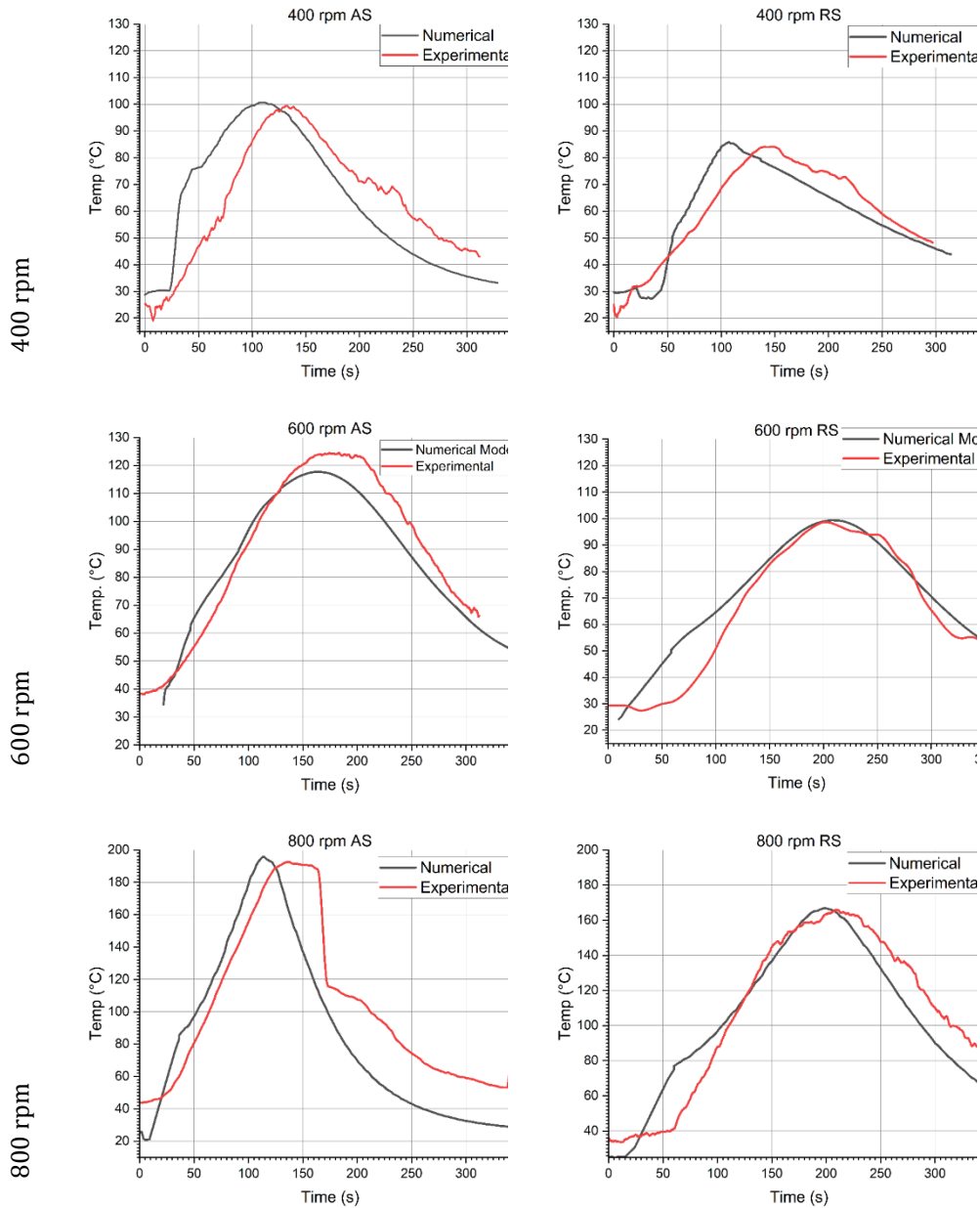
Fig. 11 *Experimental and numerical temp-time curves at various rotating speed values and a 25 mm/min travel speed*

Table 3 *NMSE as a model validation metric between the model and experimental temperatures*

	400 RS	400 AS	600 RS	600 AS	800 RS	800 AS
NMSE	1.66%	5.35%	1.58%	2.23%	1.49%	6.58%
Validity percentage	98.34%	94.65%	98.42%	97.77%	98.51%	93.42%

4.2 Joint Characterization

4.2.1 Visual Examinations

For the friction stir welded specimen at a 25 mm/min travel speed and rotation speed values of 400, 600, and 800 rpm, the visual examination shows groove formation in the top surface of the welded specimen at 400 rpm near the keyhole (Fig. 12a). Besides, the back surface shows incomplete joining between the two plates of the AA2024-T4 alloy, indicating a lower heat input than required. Whereas for the specimen welded at 800 rpm (Fig. 12c), flash is formed on the top surface along the weld-line, indicating a higher heat input than required. For the in-between condition (600 rpm), the weld is complete and almost free from flash formation (Fig. 12b). It is noticed

that the smoothness of the stir zone (SZ) top surface is higher for the larger rpm value (800) than that of 600 and 400 rpm.
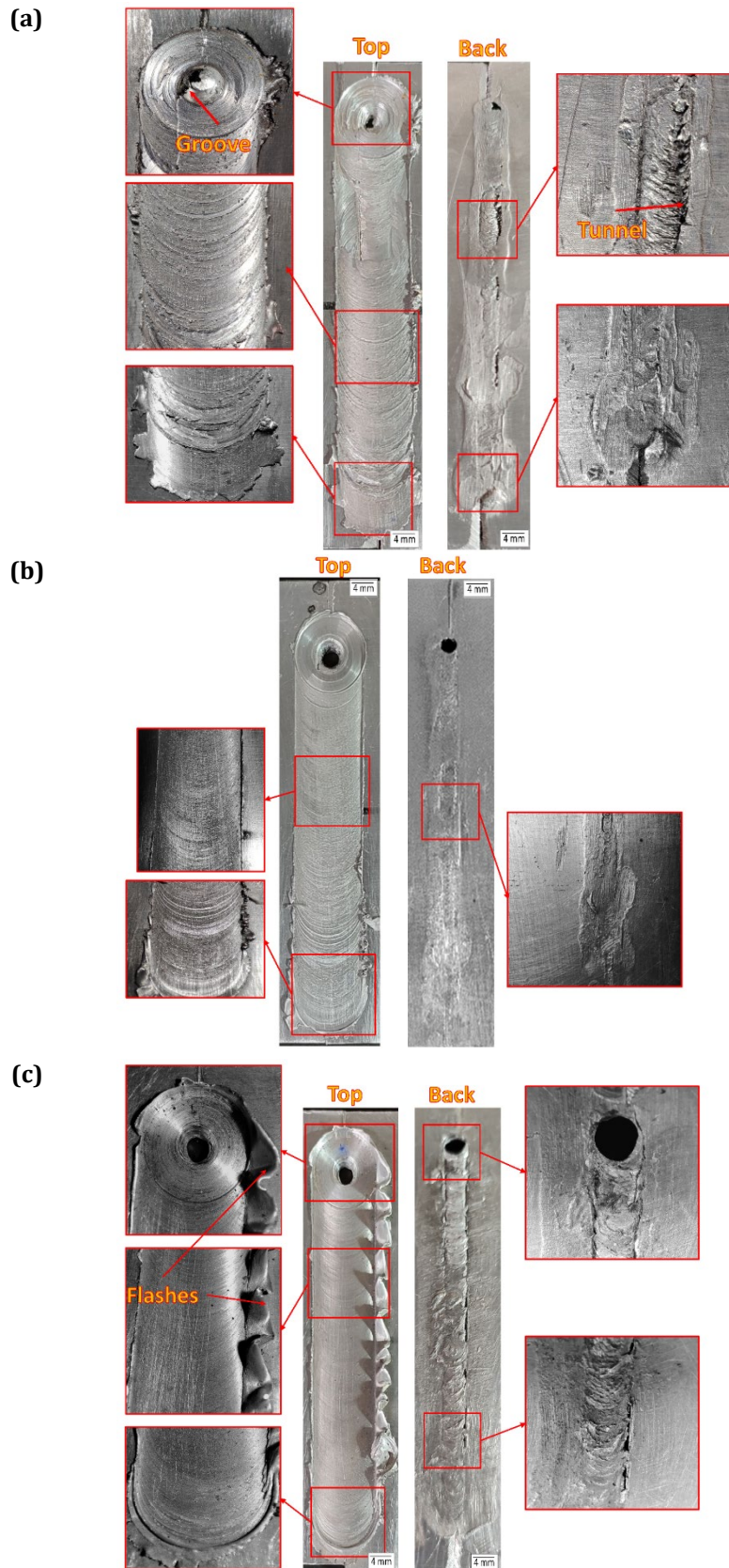

Fig. 12 *Top and back surfaces of the welded joints processed at a 25 mm/min tool travel speed and various rotation values of (a) 400 rpm; (b) 600 rpm; (c) 800 rpm*

4.2.2 Macrography and Optical Microscopy of The FSW Joints

4.2.3 Microscopic Examination

Macrographic examination of the joint cross-sections reveals the expected internal defects, such as tunnel formation inside the joint as an indication of insufficient heat input at the lowest rotational speed of 400 rpm, as given in Fig.13a, while for the optimally welded joint at 600 rpm, Fig.13b, it shows a tunnel defect-free joint.

Microstructural examination (Fig.13 and Fig.14) shows remarkable grain refinement in the stir zones for all welded specimens at all the applied FSW conditions compared to the AA2024-T4 base material (BM). HAZ has grains nearly close to the BM at low heat input (400 rpm and 25 mm/min), as give n in Fig. 13a. Whereas, its grain size is slightly larger than the BM at high heat input (800 rpm and 25 mm/min), as shown in Fig. 13c. Grains in the TMAZ have an intermediate size between the two zones since it is considered a transnational region where the thermal impact overlaps with the mechanical load from the welding tool. A lower rpm value (400) results in finer grains than higher rpm values since lower heat input means lower peak temperatures and faster cooling rates. For high rpm (above 800) grain coarsening is expected to occur or second-phase particles can get coarsened (if they exist)[8] . Equiaxed grains observed in the SZ zone for the three specimens indicate that dynamic recrystallization could occur as a result of the coexistence of thermal and mechanical conditions [12]. In addition, the microstructural images reveal that the higher rpm values led to a wider HAZ and TMAZ. Microstructural investigation also reveals the differences between the weld regions (Fig. 14) and how distinguished they are.
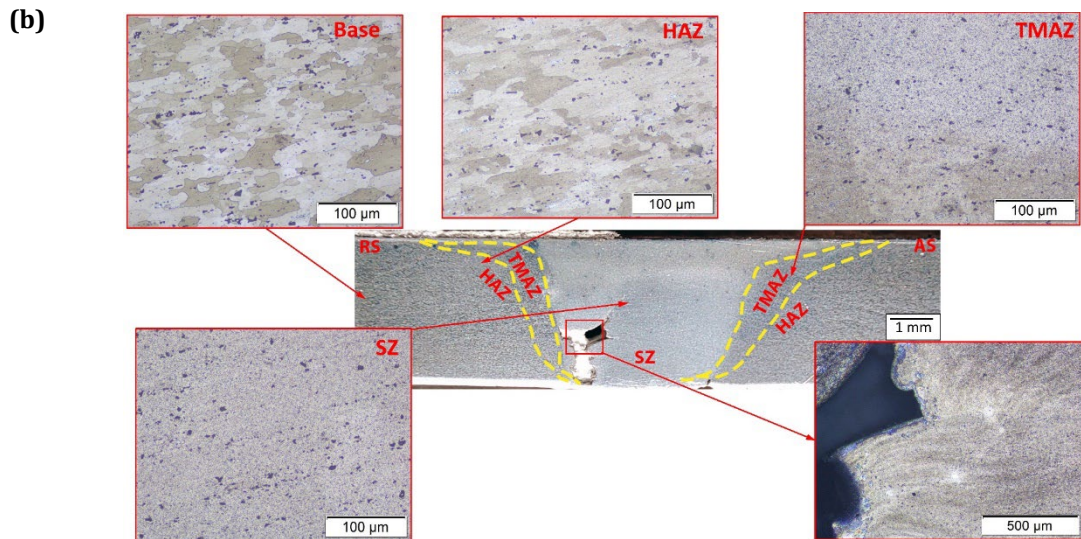
(b)
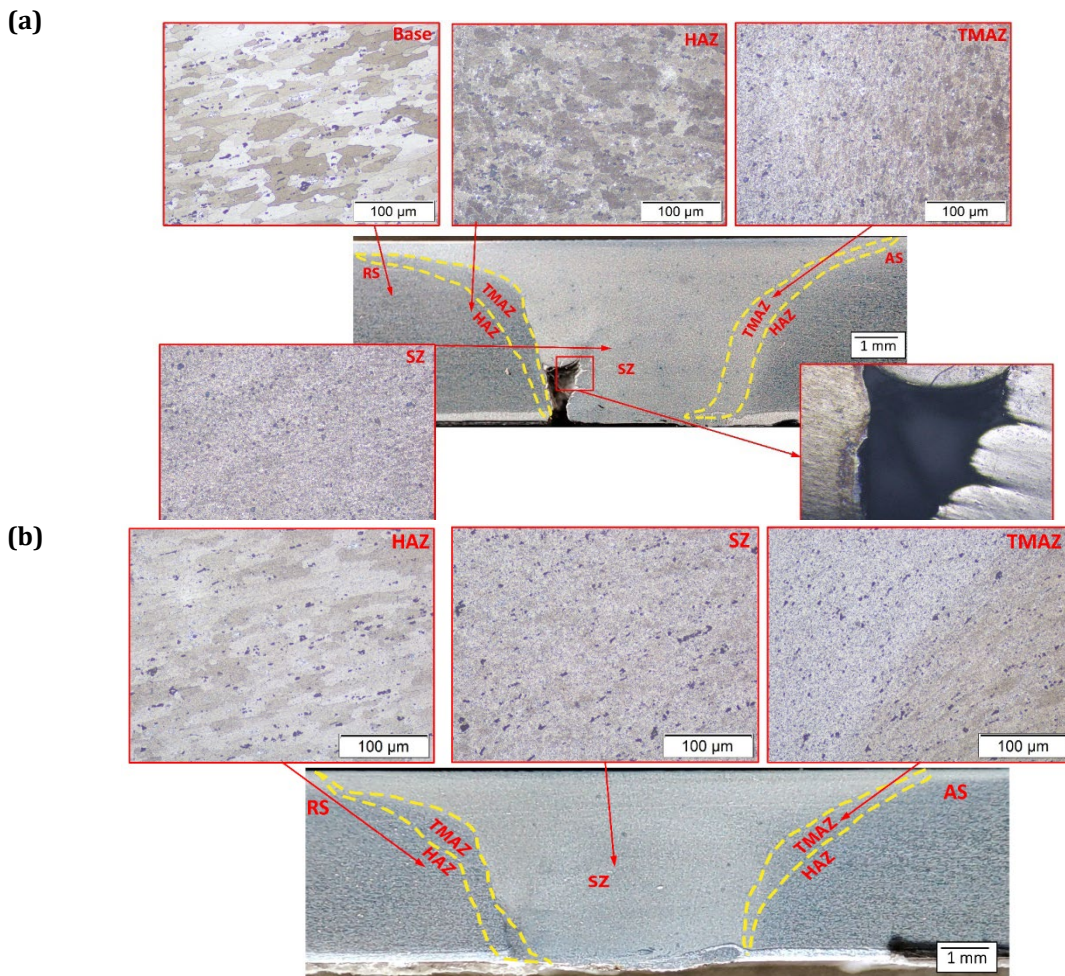
Fig. 13 *Macrography and optical microscopy images of the similar AA2024-T4 butt-joints friction stir welded at various tool rotation speeds and a constant travel speed of 25 mm/min*
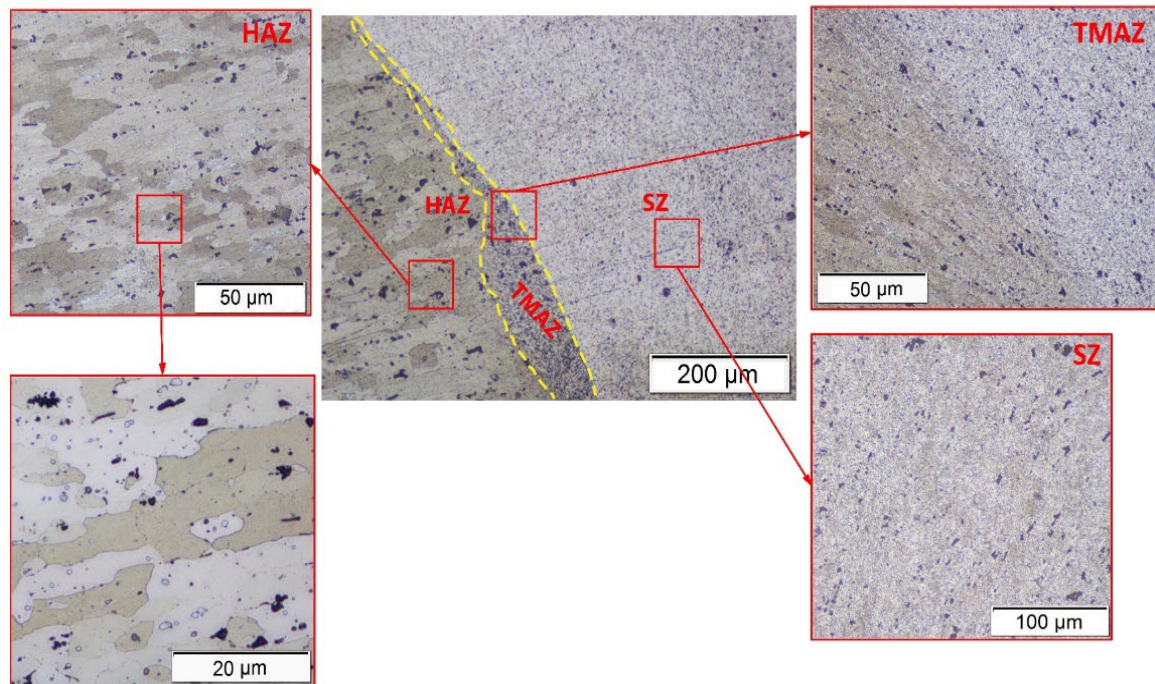

Fig 14 *Microstructure for different heat zones (HAZ, TMAZ and SZ) in the weld cross-section of the AA2024-T4 butt joints produced at 600 rpm and 25 mm/min travel speed*

4.2.4 Second Phase Analysis

A metallographic second-phase analysis was conducted according to its size and volume fraction using open-source ImageJ software. Fig. 15 shows that the rotational speed of 600 rpm gives the highest volume fraction, especially in the TMAZ, while the average particle diameter is still low (lower than that of 800 rpm), allowing more dispersion of the second phase (the least inter-particle distance). On the other hand, the 800 rpm joint gives a higher particle diameter with lower inter-particle distances meaning that second-phase coarsening could have occurred because of the excessive heating in the different weld zones [5, 8].
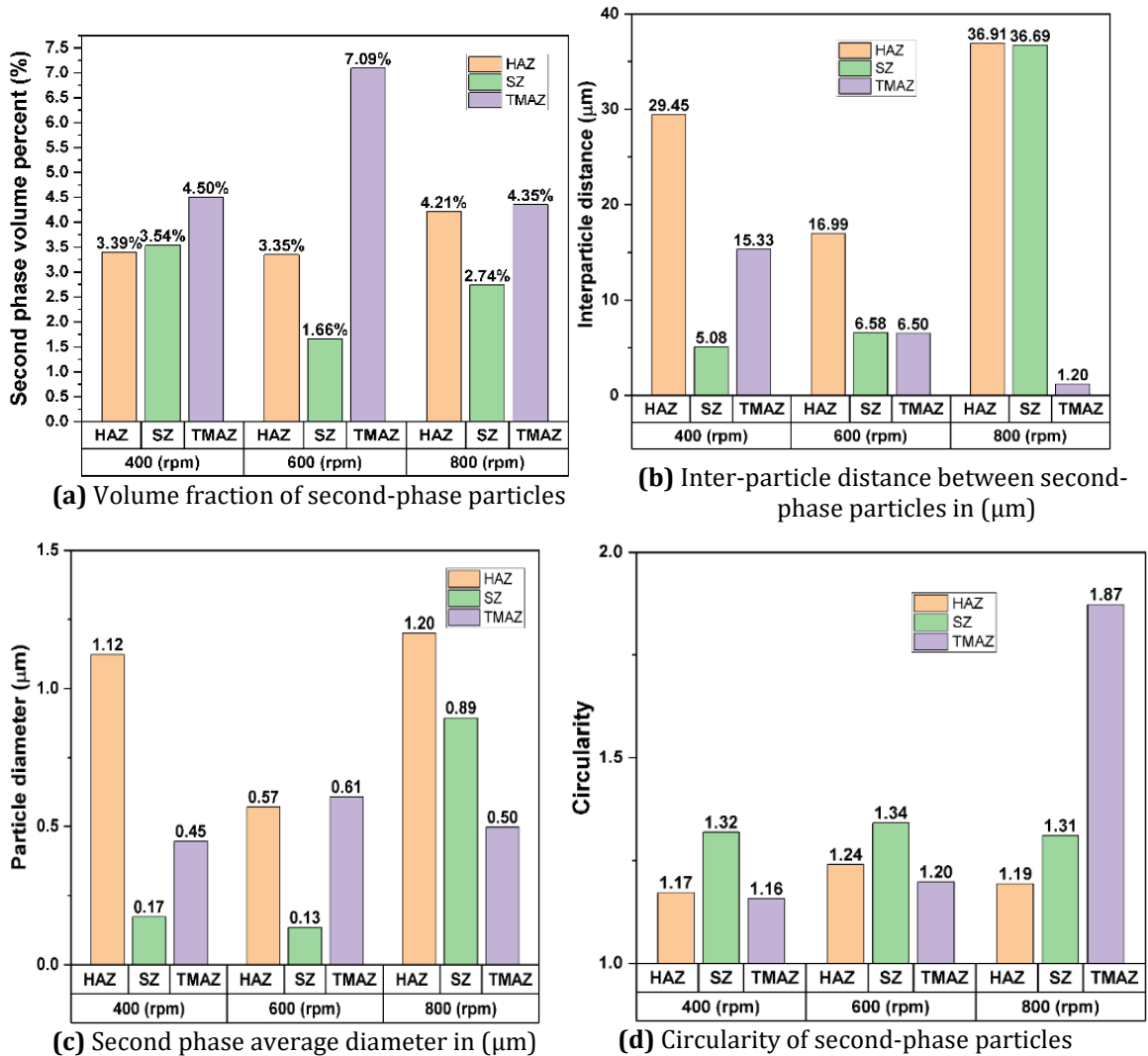
(a) Volume fraction of second-phase particles

(b) Inter-particle distance between second-phase particles in (µm)

(c) Second phase average diameter in (µm)

(d) Circularity of second-phase particles

Fig. 15 *Second-phase particle analysis (a-d) in the weld cross-section of the FSW AA2024-T4 butt joints produced at different rotation speeds and a 25 m/min travel speed*

4.2.5 Tensile Testing

Among the FSW AA 2024-T4 butt-joints that were welded at different rotation speeds, the sample processed at 600 rpm achieved the highest value of maximum ultimate tensile stress (UTS) as shown in Fig. 16. It gives about 55.5% strength efficiency relative to the UTS of BM (327 MPa). While the other two joints processed at 400 and 800 rpm attain strength efficiency of 46.3% and 51.6%, respectively. The decrease in the initial strength of the heat treated aluminum alloys when subjected to post a thermo-mechanical process is reported in previous works[8] .Two mechanisms regulate this phenomenon; decrease in grain size and presence of second-phase particles (size, morphology and volume fraction) [5, 8].

4.2.6 Tensile Test Fracture Surface

Tensile fracture has occurred in the weld zone for the three specimens indicating that the joint efficiency is less than unity. Fig. **17** shows the fracture surface of both AS and RS for the three tensile-tested specimens. A tunnel defect is observed in the welded specimen processed at 400 rpm (Fig. 17a), and it is larger than that noted for the specimen welded at 800 rpm (Fig. 17c). This type of FSW defect is not detected for the joint welded at 600 rpm (Fig. 17a). The existing tunnels in the FSW pass facilitate failure during tensile testing and reduce the joint load carrying capacity (Fig. 16). Also, there are semicircular incomplete onion rings, indicating insufficient joining near the tunnel defect area. This feature appears in welded specimens welded at 400 rpm, as multi-layered laps of metal build-up with incomplete consolidation, particularly near the weld root. Another common but less deteriorative feature is the tool marks that appear in the three specimens below the top face of the weld. Tool marks' defect is mainly attributed to the tilt and eccentric motion of the tool with striations' spacing depending on how much the tool advances per one revolution. So, these tool marks diminish as the rotational speed increases (800 rpm).
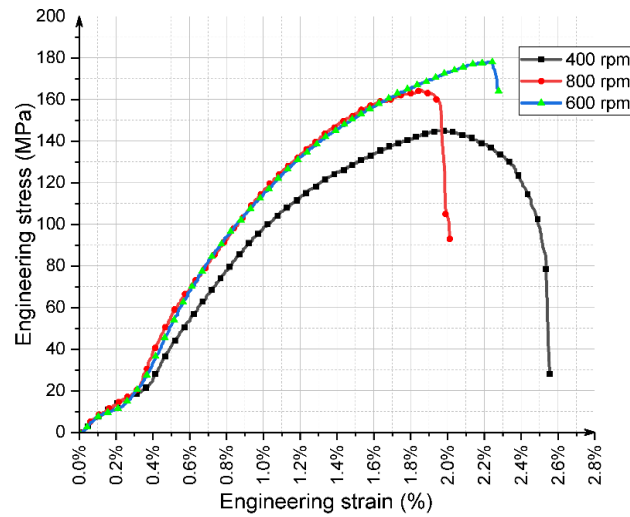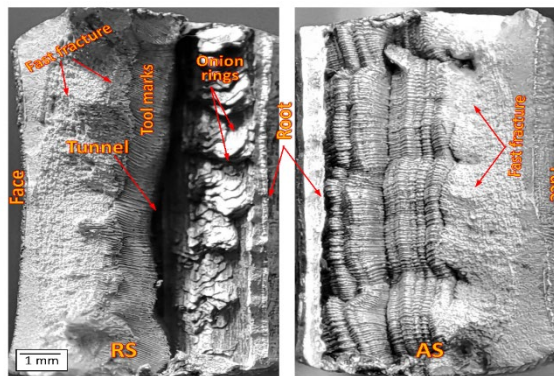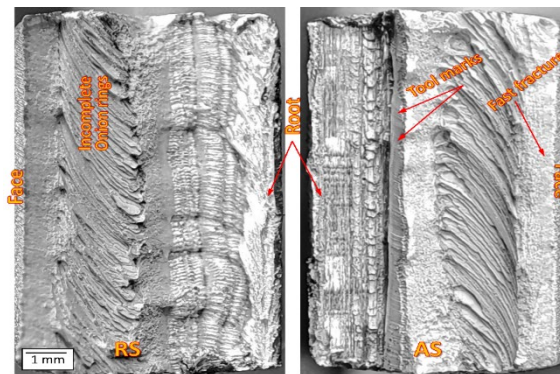
Fig. 16 *Tensile engineering stress-strain curves for the FSW AA2024-T4 butt joints at various rotation speed values (400-800 rpm) and a 25 mm/min travel speed*

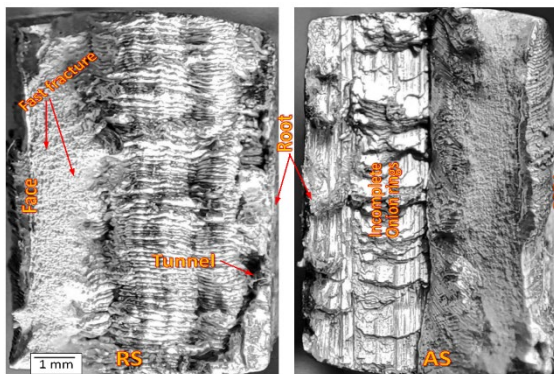**(a) 400 rpm**

(b) 600 rpm

(c) 800 rpm

Fig. 17 *Macrography of the fracture surface for the tensile test specimens of the AA2024-T4 butt joints processed at various rotation speed values and a 25 mm/min travel speed*

Penerbit
UTHM

4.2.7 Vickers Hardness

The Vickers hardness test shows the W-shaped VHN profile (Fig. 18) with higher values for the specimen welded at 600 rpm compared to the other welds processed at 400 and 800 rpm, confirming the tensile test results. For the three specimens, it is noticed that the SZ has higher hardness values compared with the HAZ and TMAZ, which indicates the impact of grain refinement effect occurring majorly in the SZ considered as the weld and heat central zone.
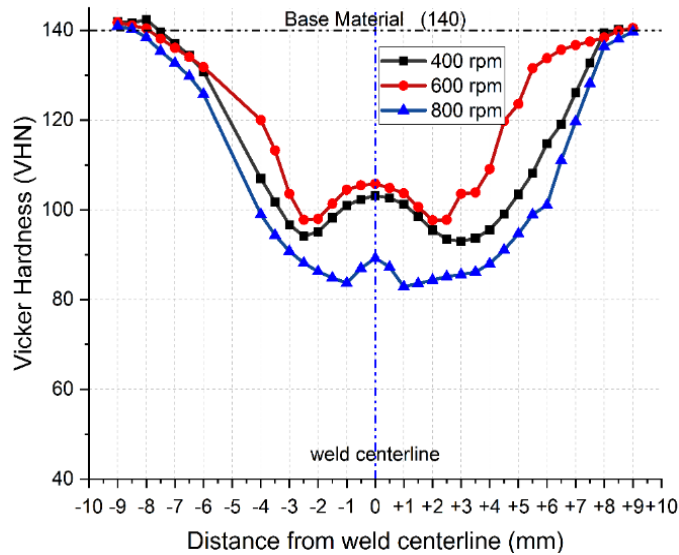

Fig. 18 *VHN curves for the FSW AA2024-T4 butt joints at various rpm values (400-600-800) and a travel speed of 25 mm/min*

5. Conclusion

- Hybrid (analytical and numerical) modelling can be employed to predict the transient heat transfer during friction stir welding of AA 2024-T4 sheets in butt joints with acceptable validation of the experimental temperature values.
- Candidate main process parameters (rotational and travel speeds) are optimized to narrow the window of the experimental validation.
- The model shows that rotational speeds less than 600 rpm give insufficient heat input, which promotes formation of tunnel and groove defects. The higher rotation values (over 600 rpm) would cause overheating and flash formation, when the optimum travel speed of 25 mm/min is applied.
- The joint with the model recommended parameters gives the defect-free joint and the best joint strength efficiency.
- Fracture surface macro-graphic examination depicts the main features and fracture-causing defects such as incomplete onion rings and tunnels.
- The Vickers hardness profile (W-shaped) for the welds' cross-sections shows that 600 rpm gives the highest values in all different welds.
- Second-phase micro-graphical analysis shows how the metal flow and dynamic recrystallization affect the redistribution and size of the second-phase particles.

Acknowledgement

Conflict of Interest

Authors declare that there is no conflict of interests regarding the publication of the paper.

Author Contribution

*The authors confirm contribution to the paper as follows: **study conception and design:** Mohamed M. El-Sayed Seleman, Ahmed M. Elnaml; **data collection:** Khalid M. Hafez; **analysis and interpretation of results:** Ahmed M. Elnaml, Sarah A. Elnekhaily, Mohamed M. Z. Ahmed; **draft manuscript preparation:** Ahmed M. Elnaml, Sabbah Ataya. All authors reviewed the results and approved the final version of the manuscript.*

References

[1]   M. M. Z. Ahmed, A. Elnaml, M. Shazly, and M. M. El-Sayed Seleman, The effect of top surface lubrication on the friction stir welding of polycarbonate sheets, *Int. Polym. Process.*, vol. 36, no. 1, pp. 94–102, Mar. 2021, doi: 10.1515/ipp-2020-3991.

[2]   V. P. Singh, S. K. Patel, A. Ranjan, and B. Kuriachen, Recent research progress in solid state friction-stir welding of aluminium–magnesium alloys: A critical review, *J. Mater. Res. Technol.*, vol. 9, no. 3, pp. 6217–6256, May 2020, doi: 10.1016/j.jmrt.2020.01.008.

[3]   M. Wade and A. P. Reynolds, Friction stir weld nugget temperature asymmetry, *Sci. Technol. Weld. Join.*, vol. 15, no. 1, pp. 64–69, Jan. 2010, doi: 10.1179/136217109X12562846839150.

[4]   N. Dialami, M. Chiumenti, M. Cervera, C. Agelet de Saracibar, and J. P. Ponthot, Material flow visualization in friction stir welding via particle tracing, *Int. J. Mater. Form.*, vol. 8, no. 2, pp. 167–181, Dec. 2015, doi: 10.1007/s12289-013-1157-4.

[5]   H. Jamshidi Aval, S. Serajzadeh, and A. H. Kokabi, Evolution of microstructures and mechanical properties in similar and dissimilar friction stir welding of AA5086 and AA6061, *Mater. Sci. Eng. A*, vol. 528, no. 28, pp. 8071–8083, Oct. 2011, doi: 10.1016/j.msea.2011.07.056.

[6]   A. A. Deshpande, D. W. J. Tanner, W. Sun, T. H. Hyde, and G. McCartney, Combined butt joint welding and post weld heat treatment simulation using SYSWELD and ABAQUS, *Proc. Inst. Mech. Eng. Part L J. Mater. Des. Appl.*, vol. 225, no. 1, pp. 1–10, Jan. 2011, doi: 10.1177/14644207JMDA349.

[7]   G. Buffa, J. Hua, R. Shivpuri, and L. Fratini, A continuum based fem model for friction stir welding - Model development, *Mater. Sci. Eng. A*, vol. 419, no. 1–2, pp. 389–396, Mar. 2006, doi: 10.1016/j.msea.2005.09.040.

[8]   M. M. E. S. Seleman, M. M. Z. Ahmed, R. M. Ramadan, and B. A. Zaki, Effect of FSW Parameters on the Microstructure and Mechanical Properties of T-joints between Dissimilar Al-Alloys, *Int. J. Integr. Eng.*, vol. 14, no. 1, pp. 1–12, 2022, doi: 10.30880/ijie.2022.14.01.001.

[9]   A. da Silva Alves, L. Mello dos Santos, P. Brito, S. Silva Ferreira de Dafé, and A. P. de Oliveira Costa, Study of Friction Stir Spot Welding Parameters for an Aluminum Alloy Aa2024- T3, *24th ABCM Int. Congr. Mech. Eng.*, no. COBEM-2017-XXIV, 2018, doi: 10.26678/abcm.cobem2017.cob17-2842.

[10]   M. Z. H. Khandkar, J. A. Khan, and A. P. Reynolds, Prediction of temperature distribution and thermal history during friction stir welding: Input torque based model, *Sci. Technol. Weld. Join.*, vol. 8, no. 3, pp. 165–174, 2003, doi: 10.1179/136217103225010943.

[11]   I. Albaijan, M. M. Z. Ahmed, M. M. El-Sayed Seleman, K. Touileb, M. I. A. Habba, and R. A. Fouad, Optimization of Bobbin Tool Friction Stir Processing Parameters of AA1050 Using Response Surface Methodology, *Materials (Basel).*, vol. 15, no. 19, p. 6886, 2022, doi: 10.3390/ma15196886.

[12]   T. Sakai, A. Belyakov, R. Kaibyshev, H. Miura, and J. J. Jonas, Dynamic and post-dynamic recrystallization under hot, cold and severe plastic deformation conditions, *Prog. Mater. Sci.*, vol. 60, no. 1, pp. 130–207, Mar. 2014, doi: 10.1016/j.pmatsci.2013.09.002.

[13]   O. S. Salih, N. Neate, H. Ou, and W. Sun, Influence of process parameters on the microstructural evolution and mechanical characterisations of friction stir welded Al-Mg-Si alloy, *J. Mater. Process. Technol.*, vol. 275, p. 116366, Jan. 2020, doi: 10.1016/j.jmatprotec.2019.116366.

[14]   N. Babu and V. Karunakaran, N Balasubramanian, Comparative evaluation of temperature distribution in GTAW and FSW joints of AA 5059 aluminium alloy, *J. Manuf. Eng.*, vol. 9, no. 2, pp. 71–76, 2014.

[15]   S. Eslami, T. Ramos, P. J. Tavares, and P. M. G. P. Moreira, Effect of Friction Stir Welding Parameters with Newly Developed Tool for Lap Joint of Dissimilar Polymers, in *Procedia Engineering*, Elsevier, 2015, pp. 199–207. doi: 10.1016/j.proeng.2015.08.059.

[16]   G. E. Schneider and M. J. Raw, Control volume finite-element method for heat transfer and fluid flow using colocated variables- 2 application and validation, *Numer. Heat Transf.*, vol. 11, no. 4, pp. 391–400, 1987, doi: 10.1080/10407788708913561.

[17]   H. Schmidt, J. Hattel, and J. Wert, An analytical model for the heat generation in friction stir welding, *Model. Simul. Mater. Sci. Eng.*, vol. 12, no. 1, pp. 143–157, Nov. 2004, doi: 10.1088/0965-0393/12/1/013.

[18]   S. Zhang, Q. Shi, Q. Liu, R. Xie, G. Zhang, and G. Chen, Effects of tool tilt angle on the in-process heat transfer and mass transfer during friction stir welding, *Int. J. Heat Mass Transf.*, vol. 125, pp. 32–42, 2018, doi: 10.1016/j.ijheatmasstransfer.2018.04.067.

[19]   M. Zhai, C. S. Wu, and H. Su, Influence of tool tilt angle on heat transfer and material flow in friction stir welding, *J. Manuf. Process.*, vol. 59, pp. 98–112, 2020, doi: 10.1016/j.jmapro.2020.09.038.

[20]   G. Rambabu, D. Balaji Naik, C. H. Venkata Rao, K. Srinivasa Rao, and G. Madhusudan Reddy, Optimization of friction stir welding parameters for improved corrosion resistance of AA2219 aluminum alloy joints, *Def. Technol.*, vol. 11, no. 4, pp. 330–337, Dec. 2015, doi: 10.1016/j.dt.2015.05.003.

[21]   A. I. Albannai, Review The Common Defects In Friction Stir Welding, *Artic. Int. J. Sci. Technol. Res.*, vol. 19, no. 11, pp. 318–329, 2020, Accessed: Feb. 07, 2023. [Online]. Available: www.ijstr.org

[22] S. Zimmer, L. Langlois, J. Laye, and R. Bigot, Experimental investigation of the influence of the FSW plunge processing parameters on the maximum generated force and torque, *Int. J. Adv. Manuf. Technol.*, vol. 47, no. 1–4, pp. 201–215, Mar. 2010, doi: 10.1007/s00170-009-2188-3.

[23] J. J. Muhsin, M. H. Tolephih, and A. M. Muhammed, Effect of friction stir welding parameters (rotation and transverse) speed on the transient temperature distribution in friction stir welding of AA 7020-t53, *ARPN J. Eng. Appl. Sci.*, vol. 7, no. 4, pp. 436–446, 2012.

[24] M. J. MohammadiSefat, H. Ghazanfari, and C. Blais, Friction Stir Welding of 5052-H18 Aluminum Alloy: Modeling and Process Parameter Optimization, *J. Mater. Eng. Perform.*, vol. 30, no. 3, pp. 1838–1850, 2021, doi: 10.1007/s11665-021-05499-5.

[25] D. Jacquin and G. Guillemot, A review of microstructural changes occurring during FSW in aluminium alloys and their modelling, *J. Mater. Process. Technol.*, vol. 288, p. 116706, Feb. 2021, doi: 10.1016/j.jmatprotec.2020.116706.

[26] V. M. J. Varghese, M. R. Suresh, and D. S. Kumar, Recent developments in modeling of heat transfer during TIG welding - A review, *Int. J. Adv. Manuf. Technol.*, vol. 64, no. 5–8, pp. 749–754, Feb. 2013, doi: 10.1007/s00170-012-4048-9.

[27] C. Yang, Q. Dai, Q. Shi, C. Wu, H. Zhang, and G. Chen, Flow-coupled thermo-mechanical analysis of frictional behaviors at the tool-workpiece interface during friction stir welding, *J. Manuf. Process.*, vol. 79, pp. 394–404, Jul. 2022, doi: 10.1016/j.jmapro.2022.05.003.

[28] A. Garg, M. Raturi, and A. Bhattacharya, Influence of additional heating in friction stir welding of dissimilar aluminum alloys with different tool pin profiles, *Int. J. Adv. Manuf. Technol.*, vol. 105, no. 1–4, pp. 155–175, Nov. 2019, doi: 10.1007/s00170-019-04186-z.

[29] A. Heidarzadeh, S. Mironov, R. Kaibyshev, G. Çam, A. Simar, A. Gerlich, F. Khodabakhshi, A. Mostafaei, D. P. Field, *et al.*, Friction stir welding/processing of metals and alloys: A comprehensive review on microstructural evolution, *Prog. Mater. Sci.*, vol. 117, p. 100752, Apr. 2021, doi: 10.1016/j.pmatsci.2020.100752.

[30] M. M. Z. Ahmed, M. I. A. Habba, M. M. El-Sayed Seleman, K. Hajlaoui, S. Ataya, F. H. Latief, and A. E. El-Nikhaily, Bobbin tool friction stir welding of aluminum thick lap joints: Effect of process parameters on temperature distribution and joints' properties, *Materials (Basel).*, vol. 14, no. 16, 2021, doi: 10.3390/ma14164585.

[31] M. Ragab, H. Liu, M. M. Z. Ahmed, G. J. Yang, Z. J. Lou, and G. Mehboob, Microstructure evolution during friction stir welding of 1Cr11Ni2W2MoV martensitic stainless steel at different tool rotation rates, *Mater. Charact.*, vol. 182, 2021, doi: 10.1016/j.matchar.2021.111561.

[32] A. P. Arakere, Computational Modeling of the Friction Stir Welding (Fsw) Process and of the Performance of Fsw, *Thesis*, 2013.

[33] H. Mohammadzadeh Jamalian, M. Tamjidi Eskandar, A. Chamanara, R. Karimzadeh, and R. Yousefian, An artificial neural network model for multi-pass tool pin varying FSW of AA5086-H34 plates reinforced with Al2O3 nanoparticles and optimization for tool design insight, *CIRP J. Manuf. Sci. Technol.*, vol. 35, pp. 69–79, Nov. 2021, doi: 10.1016/j.cirpj.2021.05.007.

[34] R. K. Uyyuru and S. V. Kallas, Numerical analysis of friction stir welding process, *J. Mater. Eng. Perform.*, vol. 15, no. 5, pp. 505–518, Oct. 2006, doi: 10.1361/105994906X136070.

[35] D. G. Andrade, C. Leitão, N. Dialami, M. Chiumenti, and D. M. Rodrigues, Analysis of contact conditions and its influence on strain rate and temperature in friction stir welding, *Int. J. Mech. Sci.*, vol. 191, p. 106095, 2021, doi: 10.1016/j.ijmecsci.2020.106095.

[36] H. S. Sanjeev, NK and Malik, Vinayak and Hebbar, Verification of Johnson-Cook Material Model Constants of Aa2024-T3 for Use in Finite Element Simulation of Friction Stir Welding and Its Utilization in Severe Plastic Deformation Process Modelling, *Int. J. Res. Eng. Technol.*, vol. 03, no. 06, pp. 98–102, Jun. 2014, doi: 10.15623/ijret.2014.0306017.

[37] S. Mandal, J. Rice, and A. A. Elmustafa, Experimental and numerical investigation of the plunge stage in friction stir welding, *J. Mater. Process. Technol.*, vol. 203, no. 1–3, pp. 411–419, Jul. 2008, doi: 10.1016/j.jmatprotec.2007.10.067.

[38] J. C. Cheng, S. Zhang, Q. Liu, S. J. Ye, S. N. Luo, Y. Cai, and J. Y. Huang, Ballistic impact experiments and modeling on impact cratering, deformation and damage of 2024-T4 aluminum alloy, *Int. J. Mech. Sci.*, vol. 224, p. 107312, 2022, doi: 10.1016/j.ijmecsci.2022.107312.

[39] A. Sarmast, S. Serajzadeh, and A. H. Kokabi, A study on thermal responses, microstructural issues, and natural aging in gas tungsten arc welding of AA2024-T4, *Proc. Inst. Mech. Eng. Part B J. Eng. Manuf.*, vol. 228, no. 3, pp. 413–421, Sep. 2014, doi: 10.1177/0954405413501669.

[40] X. K. Zhu and Y. J. Chao, Effects of temperature-dependent material properties on welding simulation, *Comput. Struct.*, vol. 80, no. 11, pp. 967–976, May 2002, doi: 10.1016/S0045-7949(02)00040-8.

[41] L. Wang, C. M. Davies, R. C. Wimpory, L. Y. Xie, and K. M. Nikbin, Measurement and simulation of temperature and residual stress distributions from friction stir welding AA2024 Al alloy, *Mater. High*

Temp., vol. 27, no. 3, pp. 167–178, 2010, doi: 10.3184/096034010X12813743510192.

[42] M. M. Z. Ahmed, M. M. E. S. Seleman, R. G. Eid, I. Albaijan, and K. Touileb, The Influence of Tool Pin Geometry and Speed on the Mechanical Properties of the Bobbin Tool Friction Stir Processed AA1050, *Materials (Basel).*, vol. 15, no. 13, 2022, doi: 10.3390/ma15134684.

[43] A. K. Choudhary and R. Jain, Fundamentals of Friction Stir Welding, Its Application, and Advancements, pp. 41–90, 2021, doi: 10.1007/978-3-030-63986-0_2.

[44] M. M. Z. Ahmed, M. I. A. Habba, N. Jouini, B. Alzahrani, M. M. El-Sayed Seleman, and A. El-Nikhaily, Bobbin tool friction stir welding of aluminum using different tool pin geometries: Mathematical models for the heat generation, *Metals (Basel).*, vol. 11, no. 3, pp. 1–19, 2021, doi: 10.3390/met11030438.

[45] S. Pal and M. P. Phaniraj, Determination of heat partition between tool and workpiece during FSW of SS304 using 3D CFD modeling, *J. Mater. Process. Technol.*, vol. 222, pp. 280–286, Aug. 2015, doi: 10.1016/j.jmatprotec.2015.03.015.

[46] R. Bhattacharjee, S. Datta, and P. Biswas, Thermomechanical and Material Flow Analysis during Friction Stir Welding of Marine Grade Aluminum Alloy 5083, *J. Sh. Prod. Des.*, vol. 39, no. 01, pp. 1–24, 2023, doi: 10.5957/jspd.02220010.

[47] R. Nandan, G. G. Roy, T. J. Lienert, and T. Debroy, Three-dimensional heat and material flow during friction stir welding of mild steel, *Acta Mater.*, vol. 55, no. 3, pp. 883–895, 2007, doi: 10.1016/j.actamat.2006.09.009.

[48] G. Ghangas, S. Singhal, S. Dixit, V. Goyat, and S. Kadiyan, Mathematical modeling and optimization of friction stir welding process parameters for armor-grade aluminium alloy, *Int. J. Interact. Des. Manuf.*, pp. 1–18, 2022, doi: 10.1007/s12008-022-01000-1.

[49] S. Kumar, M. K. Triveni, J. K. Katiyar, T. N. Tiwari, and B. S. Roy, Prediction of heat generation effect on force torque and mechanical properties at varying tool rotational speed in friction stir welding using Artificial Neural Network, *Proc. Inst. Mech. Eng. Part C J. Mech. Eng. Sci.*, 2023, doi: 10.1177/09544062231155737.

[50] Q. Liu, W. Li, L. Zhu, Y. Gao, L. Xing, Y. Duan, and L. Ke, Temperature-dependent friction coefficient and its effect on modeling friction stir welding for aluminum alloys, *J. Manuf. Process.*, vol. 84, pp. 1054–1063, 2022, doi: 10.1016/j.jmapro.2022.10.068.

[51] N. Dialami, M. Chiumenti, M. Cervera, A. Segatori, and W. Osikowicz, Enhanced friction model for Friction Stir Welding (FSW) analysis: Simulation and experimental validation, *Int. J. Mech. Sci.*, vol. 133, pp. 555–567, Nov. 2017, doi: 10.1016/j.ijmecsci.2017.09.022.

[52] N. Sabry, J. Stroh, and D. Sediako, Effects of the Friction Stir Welding Sliding and Sticking Mechanisms on the Microhardness, Texture, and Element Concentration, in *Minerals, Metals and Materials Series*, Springer, 2023, pp. 365–375. doi: 10.1007/978-3-031-22532-1_51.

[53] C. Amini, S. Hasanifard, M. Zehsaz, R. Jerez-Mesa, and J. A. Travieso-Rodriguez, Friction stir welding of AA2024-T3: development of numerical simulation considering thermal history and heat generation, *Int. J. Adv. Manuf. Technol.*, vol. 117, no. 7–8, pp. 2481–2500, May 2021, doi: 10.1007/s00170-021-07184-2.

[54] D. M. Neto and P. Neto, Numerical modeling of friction stir welding process: A literature review, *Int. J. Adv. Manuf. Technol.*, vol. 65, no. 1–4, pp. 115–126, Mar. 2013, doi: 10.1007/s00170-012-4154-8.

[55] X. Liu, Y. Yu, S. Yang, and H. Liu, A Modified Analytical Heat Source Model for Numerical Simulation of Temperature Field in Friction Stir Welding, *Adv. Mater. Sci. Eng.*, vol. 2020, p. 4639382, 2020, doi: 10.1155/2020/4639382.

[56] D. G. Andrade, C. Leitão, N. Dialami, M. Chiumenti, and D. M. Rodrigues, Modelling torque and temperature in friction stir welding of aluminium alloys, *Int. J. Mech. Sci.*, vol. 182, p. 105725, 2020, doi: 10.1016/j.ijmecsci.2020.105725.

[57] B. G. Kiral, M. Tabanoglu, and H. T. Serindag, Finite element modeling of friction stir welding in aluminum alloys joint, *Math. Comput. Appl.*, vol. 18, no. 2, pp. 122–131, 2013, doi: 10.3390/mca18020122.

[58] A. Simar, Y. Bréchet, B. De Meester, A. Denquin, C. Gallais, and T. Pardoen, Integrated modeling of friction stir welding of 6xxx series Al alloys: Process, microstructure and properties, *Prog. Mater. Sci.*, vol. 57, no. 1, pp. 95–183, 2012, doi: 10.1016/j.pmatsci.2011.05.003.

[59] D. K. Gartling, Convective heat transfer analysis by the finite element method, *Comput. Methods Appl. Mech. Eng.*, vol. 12, no. 3, pp. 365–382, Dec. 1977, doi: 10.1016/0045-7825(77)90024-X.

[60] I. Martorell, J. Herrero, and F. X. Grau, Natural convection from narrow horizontal plates at moderate Rayleigh numbers, *Int. J. Heat Mass Transf.*, vol. 46, no. 13, pp. 2389–2402, Jun. 2003, doi: 10.1016/S0017-9310(03)00010-3.

[61] G. Maragkos and T. Beji, Review of convective heat transfer modelling in cfd simulations of fire-driven flows, *Appl. Sci.*, vol. 11, no. 11, 2021, doi: 10.3390/app11115240.

[62] R. Ginell, *Tables of thermodynamic and transport properties of air, argon, carbon dioxide, carbon monoxide, hydrogen, nitrogen, oxygen and steam*, vol. 5, no. 2. US Department of Commerce, National Bureau of Standards, 1961. doi: 10.1016/0026-265x(61)90056-x.

[63]   J. H. Hattel, M. R. Sonne, and C. C. Tutum, Modelling residual stresses in friction stir welding of Al alloys—a review of possibilities and future trends, *Int. J. Adv. Manuf. Technol.*, vol. 76, no. 9–12, pp. 1793–1805, 2015, doi: 10.1007/s00170-014-6394-2.

[64]   A. A. Poli and M. C. Cirillo, On the use of the normalized mean square error in evaluating dispersion model performance, *Atmos. Environ. Part A, Gen. Top.*, vol. 27, no. 15, pp. 2427–2434, Oct. 1993, doi: 10.1016/0960-1686(93)90410-Z.

[65]   J. Ma, D. Xia, Y. Wang, X. Niu, S. Jiang, Z. Liu, and H. Guo, A comprehensive comparison among metaheuristics (MHs) for geohazard modeling using machine learning: Insights from a case study of landslide displacement prediction, *Eng. Appl. Artif. Intell.*, vol. 114, p. 105150, 2022, doi: 10.1016/j.engappai.2022.105150.